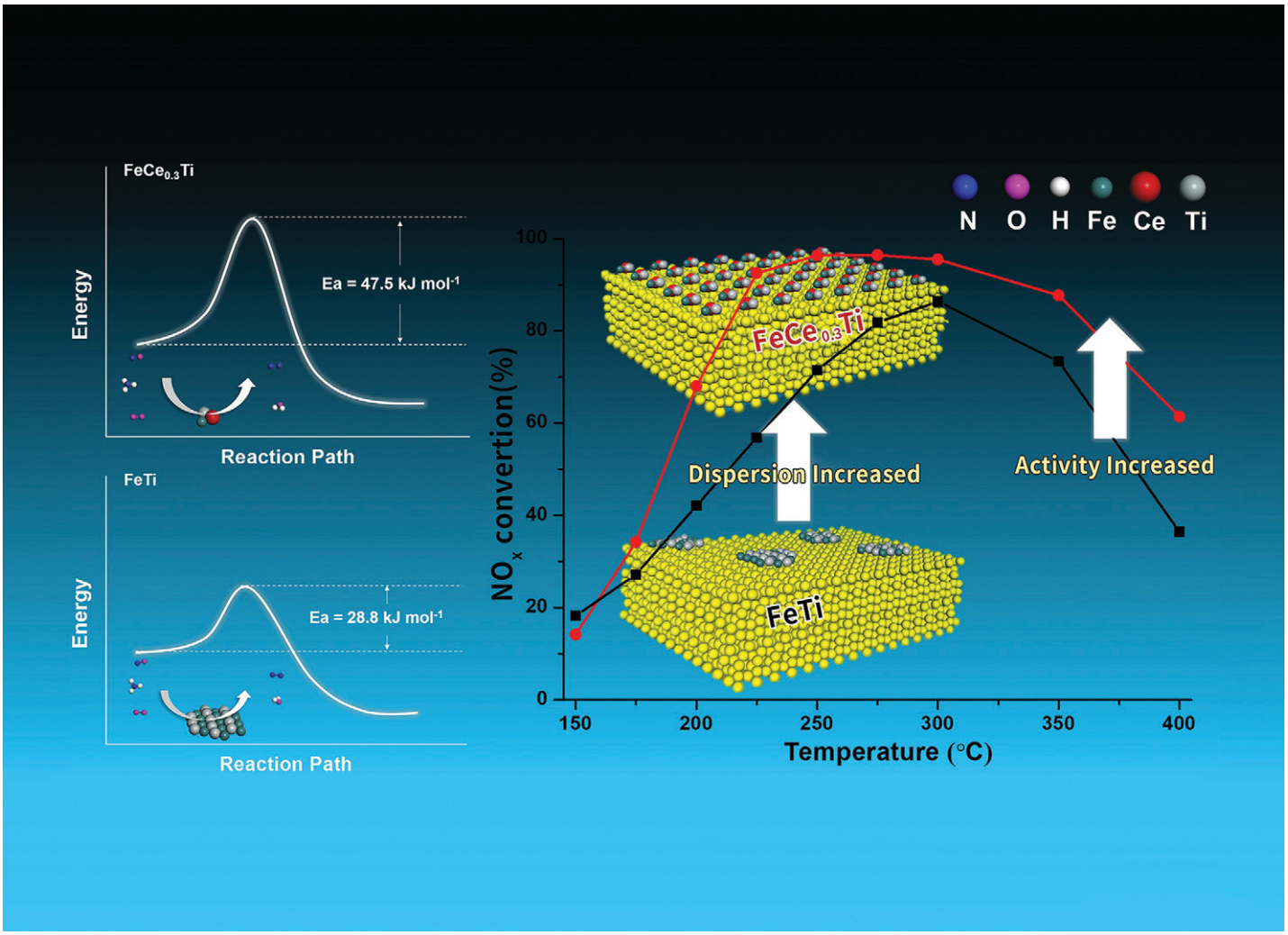

Showcasing research from Hong He's Laboratory at Research Center for Eco-Environmental Sciences, Chinese Academy of Sciences, China.

Promotion effect of cerium doping on iron–titanium composite oxide catalysts for selective catalytic reduction of NO_x with NH_3

Cerium doping weakened the redox ability and increased the activation energy of the iron-titanium composite oxide catalyst for NH_3-SCR, while promoting the dispersion of Fe and Ti, generating more active sites and achieving better NH_3-SCR activity.

As featured in:

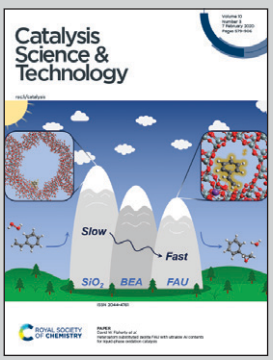

See Yunbo Yu, Hong He *et al.*, *Catal. Sci. Technol.*, 2020, **10**, 648.

ROYAL SOCIETY OF CHEMISTRY

rsc.li/catalysis

Registered charity number: 207890

Catalysis Science & Technology

ROYAL SOCIETY OF CHEMISTRY

PAPER

View Article Online
View Journal | View Issue

Cite this: *Catal. Sci. Technol.*, 2020, 10, 648

Promotion effect of cerium doping on iron–titanium composite oxide catalysts for selective catalytic reduction of NO_x with NH_3†

Wenshuo Zhang,[ab] Xiaoyan Shi,[ab] Yulong Shan,[ab] Jingjing Liu,[ab] Guangyan Xu,[ab] Jinpeng Du,[ab] Zidi Yan,[ab] Yunbo Yu *[abc] and Hong He*[abc]

A series of cerium-doped iron–titanium composite oxide catalysts ($FeCe_aTi$, a = 0.1–1.0) prepared by a urea homogeneous precipitation method were investigated for selective catalytic reduction of NO_x with NH_3 (NH_3-SCR). Over all the $FeCe_aTi$ samples, a promotion effect for NO_x reduction was induced by the introduction of cerium, with the $FeCe_{0.3}Ti$ catalyst exhibiting the best catalytic performance, even at a high GHSV of 250 000 h^{-1}. As indicated by kinetic studies, interestingly, the $FeCe_{0.3}Ti$ catalyst exhibited a higher activation energy for the NH_3-SCR process while possessing a pre-exponential factor three orders of magnitude higher than that of FeTi. Going deeper, extensive characterization including N_2-physisorption, XRD, Raman, NH_3/NO_x-TPD, XPS, EPR, and H_2-TPR was carried out. XRD and Raman results showed that the introduction of suitable amounts of Ce into the FeTi samples promoted the dispersion of Fe and Ti. Such higher dispersion of these two components increased the capacities for NO_x adsorption and activation and weakly bonded ammonia over $FeCe_{0.3}Ti$, thus promoting the occurrence of the L–H pathway of NH_3-SCR at low temperatures. H_2-TPR results indicated that the reduction of $FeCe_{0.3}Ti$ occurred at a higher temperature than that of FeTi, which may be a reason for its higher activation energy for NH_3-SCR.

Received 12th November 2019,
Accepted 26th December 2019

DOI: 10.1039/c9cy02292a

rsc.li/catalysis

Introduction

Selective catalytic reduction of NO_x with NH_3 (NH_3-SCR) is one of the most effective techniques for purifying diesel vehicle exhaust and stationary source flue gases. Much research has been carried out on preparing eco-friendly catalysts with high SCR activity. Among the developed catalysts, iron-based oxide catalysts have generated a great deal of interest in recent decades because of their low cost, abundance in nature, low toxicity, and high thermal stability compared to other metal oxide catalysts.[1–3]

For metal oxide catalysts, it is widely accepted that redox sites and acid sites working together are necessary for the process of NO_x reduction with ammonia.[4–6] Therefore, close coupling of such dual sites is highly desirable to create catalysts with high NH_3-SCR activity. With this in mind, $FeTiO_x$ composite oxide catalysts were prepared by the co-precipitation method, exhibiting higher activity than that prepared by the conventional impregnation method,[7,8] in which the Fe species served as redox sites while the Ti species acted as acid sites for ammonia adsorption. For the $FeTiO_x$ catalysts prepared by the co-precipitation method, further results achieved by X-ray absorption fine-structure (XAFS) measurements revealed that the atomic scale interaction between iron and titanium species (Fe–O–Ti structure), as a typical model of closely coupled redox and acid sites, was crucial to the SCR reaction.[9] However, the SCR activity of the Fe–Ti composite oxide catalyst at low temperatures was not high enough to be practical,[10] and its apparent activity decreased above 600 °C.[11] In view of these results, much more effort has gone into fabricating various structures of Fe (ref. 3) or Ti (ref. 12) or constructing a core–shell structure[13] for good NO_x conversion and N_2 selectivity at low temperatures. Furthermore, other kinds of metals such as Mn or Nb have been added into Fe–Ti composite oxide catalysts to obtain better SCR activity at low temperatures.[10,14,15]

In recent years, cerium oxide has received much attention in SCR catalysis due to its outstanding oxygen storage and redox properties.[16–21] Through cerium doping, the NH_3-SCR activity of FeTi mesoporous nanocatalysts and Fe-exchanged TiO_2-pillared clay was enhanced at low temperatures.[22,23] After microwave hydrothermal treatment, strong interaction

[a] *State Key Joint Laboratory of Environment Simulation and Pollution Control, Research Center for Eco-Environmental Sciences, Chinese Academy of Sciences, Beijing 100085, China. E-mail: ybyu@reccs.ac.cn, honghe@rcees.ac.cn*
[b] *University of Chinese Academy of Sciences, Beijing 100049, China*
[c] *Center for Excellence in Regional Atmospheric Environment, Institute of Urban Environment, Chinese Academy of Sciences, Xiamen 361021, China*

† Electronic supplementary information (ESI) available. See DOI: 10.1039/c9cy02292a

between Fe, Ce, and Ti and good dispersion of Fe and Ce were achieved and reported to benefit the low-temperature NH_3-SCR activity by Xiong *et al.*[24] By using the hydrothermal method, more recently, a $Fe_{0.2}Ce_{0.2}Ti_{0.6}$ catalyst was prepared by Liu *et al.*,[25] exhibiting excellent NH_3-SCR activity at a GHSV of 60 000 h^{-1}. For this catalyst, it was reported that the synergetic effect between Fe and Ce ($Ce^{4+} + Fe^{2+} \leftrightarrow Ce^{3+} + Fe^{3+}$) played a key role in the activation of both NO_x and NH_3 species, thus enhancing the de-NO_x performance, in which Ce sites contributed to the formation of NO_2 and M–NO_2 nitro species.[25] However, the aforementioned SCR activity tests and other studies about Fe–Ce–Ti composited catalysts[26,27] employed relatively low space velocities (GHSV below 120 000 h^{-1}), and the thermal stability of these FeCeTi catalysts for SCR was not intensively investigated. In addition, the effect of Ce on the structure and active sites of Fe-based composite oxide catalysts was not given much attention.

In this study, we applied a simple urea homogeneous precipitation method to add cerium into an FeTi catalyst. For the obtained $FeCe_aTi$ composite oxide catalysts, the NO_x conversion, tolerance to high space velocity and thermostability were enhanced by Ce doping. The effect of Ce modification was further investigated by the methods of N_2-physisorption, XRD, Raman, NH_3/NO_x-TPD, XPS, EPR, and H_2-TPR. The results showed that the additive Ce played multiple roles in the SCR reaction, including promoting the dispersion of Fe and Ti, increasing the amount of surface Fe and NO_x adsorption, and generating more oxygen vacancies, thus producing more active sites for the SCR reaction.

Experimental

Catalyst preparation

The urea homogeneous precipitation method was adopted to produce a series of $FeCe_aTi$ composite oxide catalysts, in which the Fe/Ti molar ratio was fixed at 1 : 1, while tuning the Ce/Ti molar ratio (a = 0.1, 0.3, 0.5, and 1.0). Typically, precursors containing $Fe(NO_3)_3{\cdot}9H_2O$, $Ce(NO_3)_3{\cdot}6H_2O$, and $Ti(SO_4)_2$ were dissolved in deionized water at the required molar ratios. Excess urea was then added into the aqueous solutions with a urea/(Fe + Ce + Ti) ratio of 10 : 1 to ensure complete precipitation. After being heated to 90 °C and being kept at this temperature for 12 h with vigorous stirring, the precipitate was filtered and washed with deionized water. The solid obtained was then dried overnight at 105 °C and calcined at different temperatures (labeled $FeCe_aTi$-600 °C and $FeCe_aTi$-700 °C for the samples calcined at 600 °C and 700 °C, respectively; others were calcined at 500 °C) for 5 h in air. For comparison, FeTi catalysts were prepared by the same procedure (labeled FeTi, FeTi-600 °C, and FeTi-700 °C for the samples calcined at 500 °C, 600 °C and 700 °C, respectively). Before NH_3-SCR activity testing, all the samples were pressed, crushed, and sieved to 40–60 mesh.

Activity tests

The NH_3-SCR activities were evaluated in fixed-bed quartz tube flow reactors with inner diameters of 4 mm (at a GHSV of 500 000 h^{-1} and 250 000 h^{-1}) and 6 mm (at a GHSV of 100 000 h^{-1} and 50 000 h^{-1}). The feed gas consisted of 500 ppm NO, 500 ppm NH_3, 5 vol% O_2, and N_2 as the balance gas, with a gas flow rate of 500 mL min^{-1}. The concentrations of NH_3, NO, NO_2, and N_2O were continually monitored using an FTIR spectrometer (IS10 Nicolet) which was equipped with a multiple-path gas cell (2 m).

The NO_x conversion and N_2 selectivity were calculated as follows:

$$\mathrm{NO}_x\,\mathrm{conversion}(\%) = \left(1 - \frac{[\mathrm{NO}_x]_{\mathrm{out}}}{[\mathrm{NO}_x]_{\mathrm{in}}}\right) \times 100\%$$

$$\mathrm{N_2\,selectivity}(\%) = \left(1 - \frac{2[\mathrm{N_2O}]_{\mathrm{out}}}{[\mathrm{NO}_x]_{\mathrm{in}} - [\mathrm{NO}_x]_{\mathrm{out}} + [\mathrm{NH_3}]_{\mathrm{in}} - [\mathrm{NH_3}]_{\mathrm{out}}}\right) \times 100\%$$

with $[NO_x] = [NO] + [NO_2]$.

Kinetic studies

The apparent activation energy (E_a) and reaction order for NO_x reduction were measured in a fixed-bed quartz tube flow reactor with an inner diameter of 4 mm. In this case, the conversion of NO_x was controlled below 25% by tuning the amount of catalyst and the total flow rate. The feed gas composition was 500 ppm NO, 500 ppm NH_3, 5% O_2, and N_2 balance.

The reaction rate of NO_x conversion was calculated as follows:

$$-R_{\mathrm{NO}_x} = \frac{F_{\mathrm{NO}_x} \times X_{\mathrm{NO}_x}}{W \times S}$$

where F_{NO_x} is the molar flow rate of NO_x, X_{NO_x} is the conversion of NO_x, W is the weight of catalyst and S is the BET surface area.

The rate of NO reduction was measured using the following kinetic equation as a function of reactant concentrations:

$$r_{\mathrm{NO}} = k[\mathrm{NO}]^{\alpha}[\mathrm{NH_3}]^{\beta}[\mathrm{O_2}]^{\gamma}$$

where r_{NO} is the SCR rate; k is the apparent rate constant; α, β, and γ are the reaction orders of NO, NH_3 and O_2, respectively. As the SCR reaction follows zero-order dependence on the partial pressure of O_2 above concentrations of 1%,[28,29] γ is 0 in our experiments. The feed gas composition was 200–1000 ppm NO, 200–1000 ppm NH_3, 5% O_2, and N_2 balance.

Catalyst characterization

N_2-Physisorption analysis was performed at 77 K using a Quantachrome Autosorb-1C instrument at liquid nitrogen temperature. The specific surface areas were calculated by

the BET equation in the 0.05–0.30 partial pressure range. The pore volumes and average pore diameters were determined by the BJH method from the desorption branches of the isotherms. Prior to each N_2-physisorption analysis, the samples were degassed at 300 °C for 3 h. Powder X-ray diffraction (XRD) patterns of the samples were measured on a Bruker D8 diffractometer with Cu Kα (λ = 0.15406 nm) radiation. The scan range of 2θ was from 20° to 90° with a step size of 0.02°. Raman spectra were recorded on a homemade UV resonance Raman spectrometer (UVR DLPC-DL-03), which was calibrated against the Stokes Raman signal of Teflon at 1378 cm^{-1}. A 532 nm He–Cd laser was used as the excitation source for the Raman measurements.

Temperature programmed desorption of ammonia or nitrogen oxide (NH_3/NO_x-TPD) experiments were carried out in a fixed-bed quartz tube flow reactor with an inner diameter of 4 mm. The concentration of NH_3/NO_x was continually monitored using an FTIR spectrometer (IS10 Nicolet) which was equipped with a multiple-path gas cell (2 m). Prior to each TPD experiment, 100 mg samples were pre-treated in 20% O_2/N_2 at a flow rate of 300 mL min^{-1} at 350 °C for 30 min, and then cooled down to 50 °C and purged with N_2 for 30 min. The samples were then exposed to a flow of 500 ppm NH_3/NO + O_2 (500 mL min^{-1}) at 50 °C for 0.5 h, followed by N_2 purging for another 0.5 h. Finally, the temperature was linearly raised to 800 °C in N_2 with a rate of 10 °C min^{-1}.

XPS measurements were carried out on an X-ray photoelectron spectrometer (AXIS Supra/Ultra) with Al Kα radiation (1486.7 eV) at an energy resolution of 0.48 eV (Ag $3d_{5/2}$). The binding energies of Fe 2p, Ce 3d, Ti 2p, and O 1s were calibrated using the C 1s peak (BE = 284.8 eV) as the standard. X-ray fluorescence analysis was carried out using a Thermo Fisher ARL Perform'X 4200 instrument with a maximum voltage of 70 KV. Electron paramagnetic resonance (EPR) spectra were obtained using a JEOL JES-FA300 spectrometer. Temperature programmed reduction with hydrogen (H_2-TPR) experiments were carried out on a Micromeritics Auto Chem 2920 chemisorption analyzer. In a typical measurement, 150 mg of the sample was firstly pretreated in a flow of 5% O_2/He with a total flow rate of 50 mL min^{-1} at 300 °C for 1 h, and then cooled to 50 °C, followed by Ar/He (1 : 1) purging for 0.5 h. Then, the temperature was linearly increased from 50 °C to 900 °C at a heating rate of 10 °C min^{-1} in a flow of 10 vol% H_2/Ar (50 mL min^{-1}), during which the H_2 consumption was continuously recorded using a thermal conductivity detector (TCD).

Results and discussion

NH_3-SCR performance

Fig. 1a shows the NO_x conversion over the FeTi and $FeCe_aTi$ catalysts in the standard SCR reaction at a high GHSV of 250 000 h^{-1}. As can be seen, the SCR activity of the FeTi catalyst was improved by Ce doping with 'a' from 0.1 to 0.5. Further increasing this value to 1.0 resulted in a decrease in the low temperature activity (<250 °C) of $FeCe_aTi$. At temperatures above 300 °C, meanwhile, the N_2 selectivity was increased by Ce doping (Fig. S1†). Among all the samples, the $FeCe_{0.3}Ti$ catalyst showed the best activity, exhibiting a NO_x conversion above 90% in a wide temperature range from 225 to 350 °C, together with a high N_2 selectivity above 85% within the whole temperature range. As a result, more attention was paid to the $FeCe_{0.3}Ti$ catalyst in the following study, in comparison with the FeTi catalyst. After calcining at the higher temperatures of 600 °C and 700 °C, the activity of $FeCe_{0.3}Ti$ and FeTi was also measured, with the results shown in Fig. 1b. Within the whole temperature range, the NO_x conversion of the FeTi-600 °C catalyst was much lower than that of the one calcined at 500 °C in Fig. 1a, with only a 58% NO_x conversion at 300 °C. As for $FeCe_{0.3}Ti$, however, such deterioration induced by calcination at the temperature of 600 °C was suppressed markedly, with a NO_x conversion of 98% at 300 °C, indicative of higher thermostability. When the calcination temperature was further increased to 700 °C, the NO_x conversion over both catalysts decreased significantly. In addition, as shown in Fig. S2,† the $FeCe_{0.3}Ti$ catalyst presented much better resistance to high space velocities than FeTi.

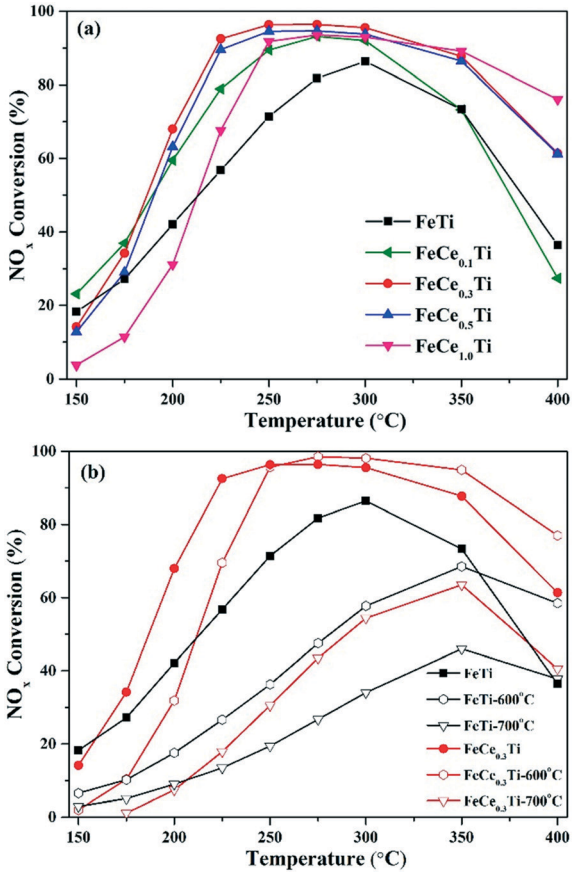

Fig. 1 NO_x conversion over (a) FeTi and $FeCe_aTi$ catalysts calcined at 500 °C and (b) $FeCe_{0.3}Ti$ and FeTi catalysts calcined at 500 °C, 600 °C, and 700 °C, respectively. Reaction conditions: [NO] = [NH_3] = 500 ppm, [O_2] = 5 vol%, N_2 balance, GHSV = 250 000 h^{-1}.

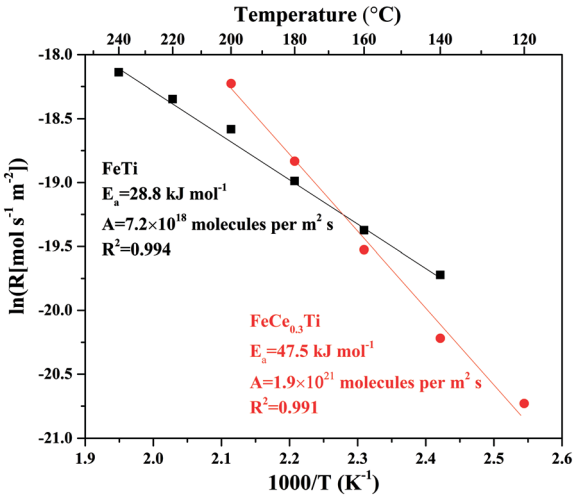

Fig. 2 Arrhenius plots of the reaction rates over the FeTi and $FeCe_{0.3}Ti$ catalysts calcined at 500 °C. Reaction conditions: [NO] = $[NH_3]$ = 500 ppm, $[O_2]$ = 5 vol%, N_2 balance.

Kinetic studies

To further investigate the influence of cerium doping on the SCR activity of the FeTi catalyst, kinetic experiments were carried out. Fig. 2 shows the Arrhenius plots of the reaction rates for NO_x reduction within the temperature range of 120–240 °C; the apparent activation energies (E_a) were obtained from the slope of the fitted curve. The E_a of the $FeCe_{0.3}Ti$ catalyst was 47.5 kJ mol^{-1}, which is higher than that of FeTi (28.8 kJ mol^{-1}). It should be noted that, however, the pre-exponential factor (A) for $FeCe_{0.3}Ti$ was 1.9×10^{21} molecules per m^2 s, which is three orders of magnitude higher than that of FeTi (7.2×10^{18} molecules per m^2 s). This result clearly revealed that more active sites were available for NO_x reduction over the $FeCe_{0.3}Ti$ sample.[30] Further kinetic experiments were carried out over the FeTi and $FeCe_{0.3}Ti$ catalysts calcined at 600 °C and 700 °C, respectively, with the results shown in Fig. S3 and Table S1.† In this case, the $FeCe_{0.3}Ti$ catalysts always showed a higher E_a and larger 'A' than the FeTi catalysts as expected.

During the NH_3-SCR reactions, the dependence of the NO_x reduction rate on the concentrations of NO and NH_3 was also measured at 150 °C (Fig. 3). For the $FeCe_{0.3}Ti$ catalyst in Fig. 3a, the reaction order of NO (α) was 0.44, which is much lower than that of FeTi (α = 0.71). This result strongly suggests that larger amounts of NO were adsorbed on $FeCe_{0.3}Ti$ and took part in the SCR reaction.[29,31] At a given NO concentration, the $FeCe_{0.3}Ti$ sample exhibited a much higher reaction rate for NO_x reduction than the Ce-free sample, which is in good agreement with the results indicated by the pre-exponential factor. From Fig. 3b, it can be easily observed that the reaction order of NH_3 is zero over both the FeTi and $FeCe_{0.3}Ti$ catalysts, indicating that ammonia involved in the SCR reaction is always in the adsorbed form.[28,29] These results suggested that over both samples, the L–H reaction pathway occurred during the NH_3-SCR process at low temperatures, particularly over the

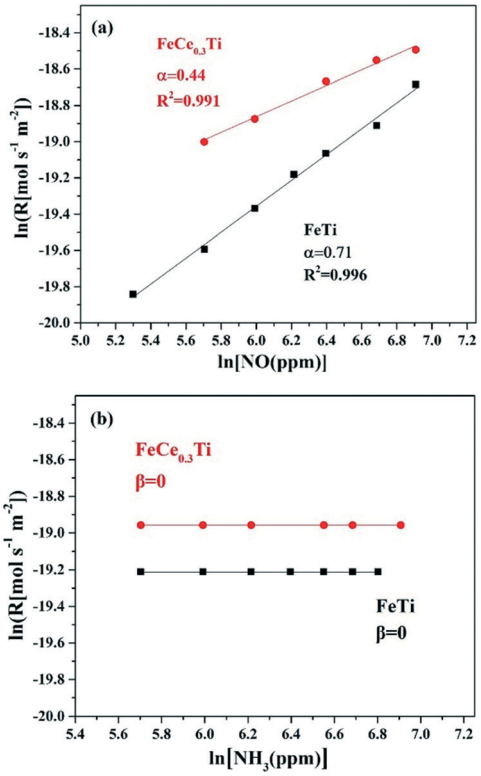

Fig. 3 The dependence of NO_x reduction rate on the concentrations of (a) NO and (b) NH_3 at 150 °C over the FeTi and $FeCe_{0.3}Ti$ catalysts calcined at 500 °C. Reaction conditions: (a) $[NH_3]$ = 500 ppm, [NO] = 200–1000 ppm; (b) [NO] = 500 ppm, $[NH_3]$ = 200–1000 ppm, $[O_2]$ = 5 vol%, N_2 balance.

$FeCe_{0.3}Ti$ catalyst. Also, the $FeCe_{0.3}Ti$ catalyst showed a higher reaction rate of 5.8×10^{-9} mol m^{-2} s^{-1}, which was higher than that of FeTi (4.5×10^{-9} mol m^{-2} s^{-1}).

Structural properties

N_2-Physisorption analysis. The BET surface area, pore volume, and average pore diameter of the catalysts are listed in Table 1. Adding a small amount of Ce (a = 0.1) into the FeTi catalyst increased the surface area from 147 to 188 m^2 g^{-1}, which was accompanied by a slight increase in pore volume and a decrease in pore diameter. However, as the

Table 1 Structural parameters of FeTi and $FeCe_aTi$ catalysts calcined at 500 °C, 600 °C, and 700 °C, respectively

	Surface area (m^2 g^{-1})	Pore volume (cm^3 g^{-1})	Pore diameter (nm)
FeTi	147	0.27	4.9
$FeCe_{0.1}Ti$	188	0.29	3.8
$FeCe_{0.3}Ti$	151	0.20	3.4
$FeCe_{0.5}Ti$	139	0.19	3.4
$FeCe_{1.0}Ti$	88	0.13	3.4
$FeCe_{0.3}Ti$-600 °C	78	0.18	4.9
$FeCe_{0.3}Ti$-700 °C	76	0.16	3.1
FeTi-600 °C	84	0.23	9.6
FeTi-700 °C	27	0.10	3.4

doping amount of Ce further increased, the surface area, pore volume, and pore diameter of the $FeCe_aTi$ catalysts decreased gradually. The surface area of $FeCe_{0.3}Ti$ was 151 $m^2\ g^{-1}$, being close to that of the FeTi catalyst (147 $m^2\ g^{-1}$). After calcining these two samples at 600 °C, their surface areas decreased dramatically; nevertheless, they have similar values. Upon further increasing the calcination temperature from 600 °C to 700 °C, the surface area of $FeCe_{0.3}Ti$ hardly changed, while that of FeTi decreased considerably.

XRD analysis. Fig. 4a shows the XRD patterns of the FeTi and $FeCe_aTi$ catalysts calcined at 500 °C. As for the FeTi catalyst, the diffraction peaks of hematite Fe_2O_3 and pseudobrookite Fe_2TiO_5 were observed. Adding a small amount of cerium (a = 0.1–0.3) into the FeTi sample resulted in a decrease in the intensities of peaks related to hematite Fe_2O_3 and pseudobrookite Fe_2TiO_5. This result indicated that the crystallization of these two phases was suppressed by cerium doping. With a further increase in the cerium doping amount, the diffraction peaks of fluorite-structured cubic CeO_2 appeared for the $FeCe_{0.5}Ti$ and $FeCe_{1.0}Ti$ catalysts, which may be a reason for the decreased SCR activity and agrees well with the results by Long *et al.* that well-dispersed cerium improves the SCR activity.[22] Among all the samples calcined at 500 °C, it should be noted that the lowest intensity of Fe_2O_3 and Fe_2TiO_5 was observed for $FeCe_{0.3}Ti$ and no peak related to Ce appeared, indicating that both Fe and Ce were highly dispersed or in an amorphous state. For all the catalysts, interestingly, no peak of individual titanium oxides appeared, indicative of their highly-dispersed amorphous state. As for the $FeCe_{0.3}Ti$-600 °C catalyst (Fig. 4b), peaks of hematite Fe_2O_3, pseudobrookite Fe_2TiO_5, and cubic CeO_2 were observed, exhibiting higher intensity compared with those of the corresponding sample calcined at 500 °C. This difference possibly results in a lower NO_x conversion of the former at temperatures below 250 °C than that of the latter. Further increasing the calcination temperature to 700 °C strengthened the peak intensities of these three phases, which was accompanied by the appearance of rutile TiO_2, indicating serious phase separation of Fe, Ce, and Ti oxides. As the surface areas of $FeCe_{0.3}Ti$-600 °C and $FeCe_{0.3}Ti$-700 °C were similar, this phase separation may be a reason for the observation of decreased activity after calcining at higher temperatures. Rutile TiO_2 was also detected in FeTi-600 °C and FeTi-700 °C, exhibiting much higher intensity than that for $FeCe_{0.3}Ti$ calcined at the same temperature, respectively (Fig. S4†), suggesting that more serious phase separation of Fe and Ti oxides occurred in the FeTi catalyst. This result in turn reveals that the introduction of Ce into the FeTi samples in suitable amounts promoted the dispersion of Fe and Ti, thus providing more active sites available for the SCR process and contributing to higher activity, which was also shown by Qu *et al.* in a previous investigation.[32]

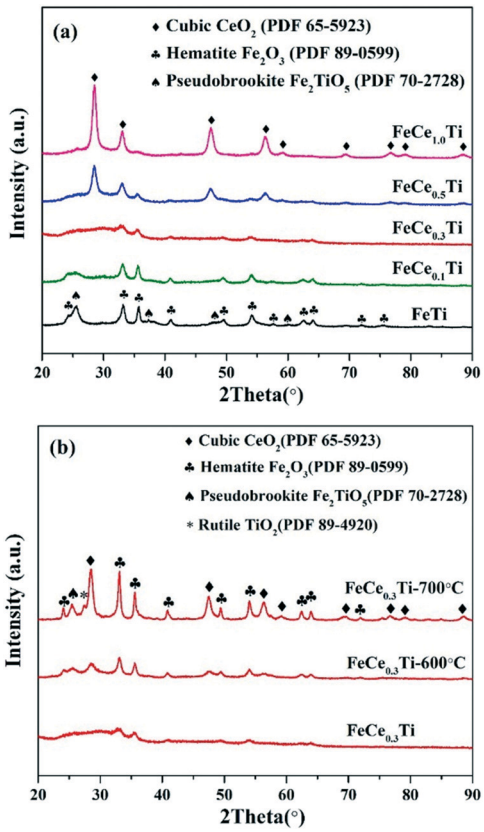

Fig. 4 XRD patterns of (a) FeTi and $FeCe_aTi$ catalysts calcined at 500 °C and (b) $FeCe_{0.3}Ti$ catalysts calcined at 500 °C, 600 °C, and 700 °C.

Raman analysis. Visible wavelength Raman spectroscopy was applied to investigate the lattice vibrational states of the catalysts, with the results shown in Fig. 5. For all the samples, the peaks ascribed to the E_g mode of hematite (α-Fe_2O_3) appeared at 292, 400, 516, and 658 cm^{-1}, together with a peak at 1332 cm^{-1} ascribed to the second harmonic vibration for phonon scattering of α-Fe_2O_3.[33,34] For the $FeCe_{0.5}Ti$ and $FeCe_{1.0}Ti$ catalysts, a strong peak assignable to the F_{2g} symmetry mode of the CeO_2 phase at 457 cm^{-1} was observed.[35,36] As for the spectra of the $FeCe_{0.3}Ti$-600 °C and

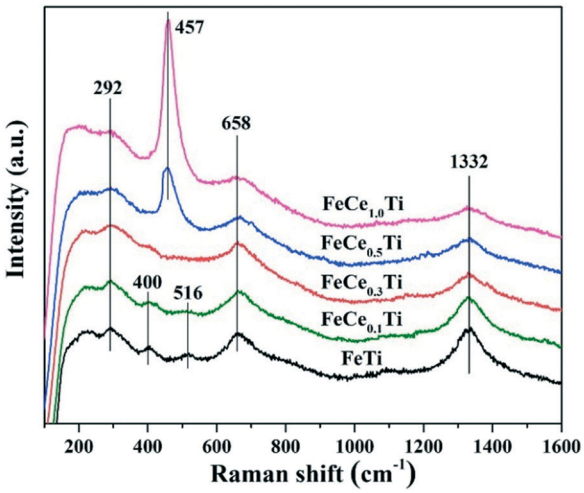

Fig. 5 Raman spectra of FeTi and $FeCe_aTi$ catalysts calcined at 500 °C.

$FeCe_{0.3}Ti$-700 °C catalysts shown in Fig. S5,† peaks due to α-Fe_2O_3 were also observed at 659 and 1332 cm^{-1}, together with the appearance of peaks for rutile TiO_2 (238 cm^{-1}) and Fe_2TiO_5 (437 and 797 cm^{-1}), respectively.[37] These results are in good accordance with the XRD measurements.

Adsorption/desorption properties

NH_3-TPD analysis. To distinguish the surface acid properties of the FeTi and $FeCe_aTi$ catalysts, NH_3-TPD analysis was performed for the samples, with the results shown in Fig. 6. During the experiment, the total desorption amount of NH_3 of each sample was calculated and is also shown in Fig. 6. The introduction of a small amount of Ce (a = 0.1) into FeTi increased the total desorption amount of NH_3, indicating an increase in the relative quantity of surface acid sites. Such increase may derive from the increased surface area, as listed in Table 1. With a further increase of 'a' from 0.3 to 1.0, the total amount of NH_3 desorption decreased gradually, also indicating the influence of surface area on NH_3 adsorption. It is well accepted that the adsorption of ammonia is the initial step in the NH_3-SCR process. The $FeCe_{0.3}Ti$ and FeTi samples exhibited almost the same ammonia adsorption capacities (Fig. 6) and BET surface areas (Table 1), while the former exhibited higher intrinsic activity for NO_x reduction (Fig. 3). As a result, it is not the ammonia adsorption capacity that governs the catalytic performance of these two catalysts. Such a conclusion was also indicated by the results in Fig. 3b, in which the reaction order of ammonia is zero, suggesting that large amounts of ammonia were adsorbed on these two samples that were sufficient for the occurrence of the NH_3-SCR process. Our results are also in good agreement with the recent finding achieved on V-based catalysts, which is not all the adsorbed ammonia species participate in the NH_3-SCR process simultaneouly.[38,39]

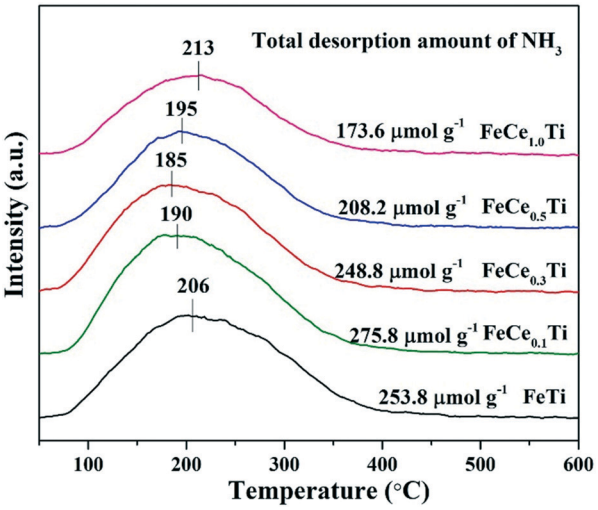

Fig. 6 NH_3-TPD results of FeTi and $FeCe_aTi$ catalysts calcined at 500 °C.

With the introduction of Ce, it should be noted that the desorption peak of NH_3 shifted to low temperature gradually, reaching the lowest value of 185 °C over the $FeCe_{0.3}Ti$ catalyst, and then rose with the further increase of 'a'. This indicated that more weak-acid sites on the $FeCe_{0.3}Ti$ catalyst were available for NH_3 adsorption compared to those on the other catalysts, and thus resulted in weaker bonding between adsorbed ammonia and acid sites. With the Sabatier principle in mind, such weak interaction would be just right for the reaction of ad-NH_3 with ad-NO_x (or NO_x in the gas phase) at low temperatures. As a result, it is reasonable that $FeCe_{0.3}Ti$ is more active for NO_x reduction than FeTi. Generally, the stability of NH_4^+ species bonded on Brønsted acid sites is weaker than that of NH_3 molecules coordinated to Lewis acid sites,[40,41] and therefore it can be supposed that more weak Brønsted acid sites existed on the $FeCe_{0.3}Ti$ catalyst, which is beneficial for the L–H mechanism pathway of NH_3-SCR.[42]

NO_x-TPD analysis. To further investigate the adsorption and activation behaviors of NO_x species over the FeTi and $FeCe_{0.3}Ti$ catalysts calcined at 500 °C, NO_x-TPD experiments were performed and the desorption amounts of NO and NO_2 were calculated, respectively. As shown in Fig. 7, three desorption peaks appeared for both catalysts. The NO_x desorption peaks around 124 °C were due to the

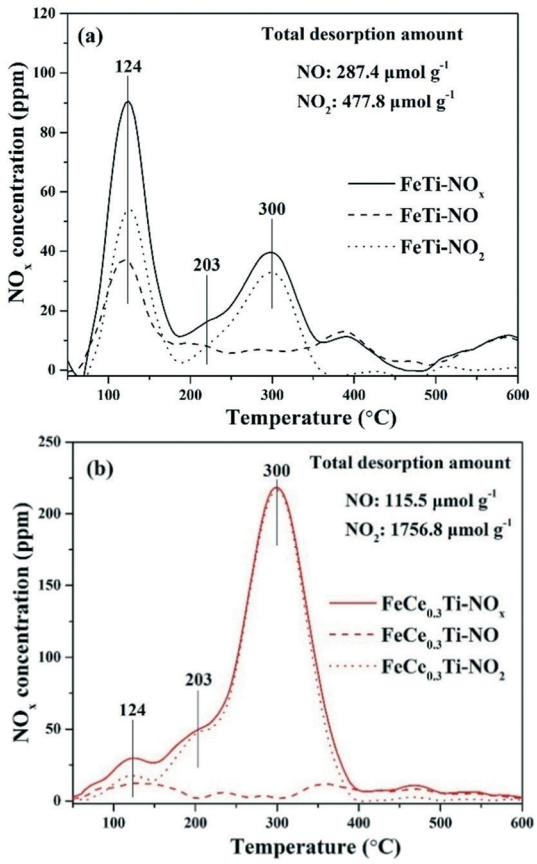

Fig. 7 NO_x-TPD results of (a) FeTi and (b) $FeCe_{0.3}Ti$ catalysts calcined at 500 °C.

decomposition of monodentate nitrate, the peaks around 203 °C were ascribed to the weakly adsorbed bridging nitrate and the peaks around 300 °C were attributed to bidentate and bridging nitrate, with higher thermal stability.[10,43] Within all temperature ranges, it is clear that much more NO_2 was desorbed from the $FeCe_{0.3}Ti$ catalyst than from FeTi, indicating that the adsorbed NO_x species on the $FeCe_{0.3}Ti$ catalyst were mainly NO_3^- species.[44] It was reported that the Fe sites on the FeTi catalyst contributed to NO_x adsorption during the NH_3-SCR process.[43] As revealed in Table 2, Ce doping greatly promoted the surface enrichment of Fe species. Taking these results into account, we can expect that the introduction of Ce into the FeTi samples should enhance the NO_x adsorption ability. As expected, the total desorption amount of NO_x from the $FeCe_{0.3}Ti$ catalyst was 1872.3 μmol g^{-1}, which was 2.4 times that from the FeTi catalyst (765.2 μmol g^{-1}). This result was also in accordance with the conclusions reached from kinetic studies.

Redox behavior

XPS analysis. The Fe 2p, Ce 3d, Ti 2p, and O 1s XPS results for the samples are shown in Fig. 8. Over all the samples, peaks corresponding to Fe 2p1/2 and Fe 2p3/2 were observed at around 724.5 eV and 711.2 eV, respectively (Fig. 8a), exhibiting decreased intensity with increasing Ce content, which was due to the reduced relative amount of Fe. Such tendency was further confirmed by the peak located at 719.4 eV assigned to the Fe 2p3/2 satellite peak.[13,29,45] As shown in Fig. 8b, peaks at around 464.1 eV and 458.3 eV were observed for all the samples, ascribed to Ti 2p1/2 and Ti 2p3/2, respectively.[46,47] The intensity of the Ti 2p peaks was also decreased upon adding Ce due to the reduction in the relative amount of Ti.

Fig. 8c shows the Ce 3d XPS spectra of all the samples containing Ce, and each spectrum was deconvoluted into eight peaks. The binding energies of these peaks are listed in Table S4,† in which the peaks labeled u_1 and v_1, representing the $3d^{10}4f^1$ initial electronic state, corresponded to Ce^{3+}, and the peaks labeled u, u_2, u_3, v, v_2, and v_3 represented the $3d^{10}4f^0$ state of Ce^{4+}, according to previous investigations.[18,48,49] It is well accepted that oxygen vacancies can be produced by the transformation between Ce^{3+} and Ce^{4+}, $4Ce^{4+} + O^{2-} \rightarrow 2Ce^{4+} + 2Ce^{3+} + \square + 0.5O_2$ (□ represents an empty position).[50] With this in mind, we can deduce that the higher the concentration of Ce^{3+}, the higher the density of oxygen vacancies. To highlight this issue, the $Ce^{3+}/(Ce^{3+} + Ce^{4+})$ ratios were calculated from the peak areas and are presented in Table 2. Among all the Ce-containing samples, noticeably, the $FeCe_{0.3}Ti$ catalyst exhibited the highest ratio of Ce^{3+} (16.6%), indicating the largest amount of oxygen vacancies,[18,49] which is favorable for NO adsorption and contributes to SCR activity.[35,51,52] The formation of oxygen vacancies was further proven by EPR experiments in Fig. S6,† in which the $FeCe_{0.3}Ti$ catalyst showed the strongest intensity of typical signal of electrons trapped in oxygen vacancies, being in agreement with the result of XPS.[53,54]

The O 1s XPS spectra of the FeTi and $FeCe_aTi$ catalysts are shown in Fig. 8d, in which each spectrum has been deconvoluted into two peaks. For FeTi, the peak at 531.1 eV was assignable to surface oxygen (O_2^{2-} or O^-, denoted as O_α thereafter), whereas the peak at 530.0 eV was ascribed to lattice oxygen (O^{2-}, denoted as O_β thereafter).[55,56] With Ce addition, it was noted that the peak of O_β shifted to lower binding energy, which may due to the stronger interactions between Ce and O.[57] Generally, the surface oxygen is more active in oxidation reactions than lattice oxygen. As a result, the ratio of $O_\alpha/(O_\alpha + O_\beta)$ was calculated, with the results shown in Table 2. Notably, the ratio of $O_\alpha/(O_\alpha + O_\beta)$ on the $FeCe_{0.3}Ti$ catalyst was up to 52.4%, which was much higher than that on the FeTi sample (34.6%) and other Ce-containing samples. This result indicated that the addition of Ce increased the percentage of O_α and promoted the oxidation of NO.[10,58–60]

Based on the XPS and XRF measurements (Table S2†), furthermore, the ratios of Fe/Ti on the surface and in the bulk phase were calculated, with the results listed in Table 2. It is worth noting that the ratios of Fe/Ti in the bulk phase of the FeTi and $FeCe_aTi$ catalysts were almost the same and in good accordance with the nominal value (Fe/Ti = 1 : 1). For these samples, however, the ratio of Fe/Ti near the surface is much higher than that in the bulk phase, indicative of surface enrichment of Fe species. Particularly for Ce-containing samples, such surface enrichment was more pronounced. This result indicated that the addition of Ce increased the surface Fe concentration, and thus ensured sufficient active sites for redox cycling,[35] which is in accordance with the results of the kinetic studies mentioned above.

Table 2 Surface and bulk components of FeTi and $FeCe_aTi$ catalysts calcined at 500 °C

	Bulk Fe/Ti[a]	Surface Fe/Ti[b]	Surface $Ce^{3+}/(Ce^{3+} + Ce^{4+})$	Surface $O_\alpha/(O_\alpha + O_\beta)$
FeTi	1.08	7.9	—	34.6%
$FeCe_{0.1}Ti$	1.07	10.1	15.1%	36.5%
$FeCe_{0.3}Ti$	1.06	13.3	16.6%	52.4%
$FeCe_{0.5}Ti$	1.06	15.5	15.9%	50.7%
$FeCe_{1.0}Ti$	1.08	17.8	9.5%	43.5%

[a] Atom ratios in the bulk phase of catalysts calculated from XRF in Table S2.† [b] Atom ratios in the near-surface region of catalysts calculated from XPS in Table S3.†

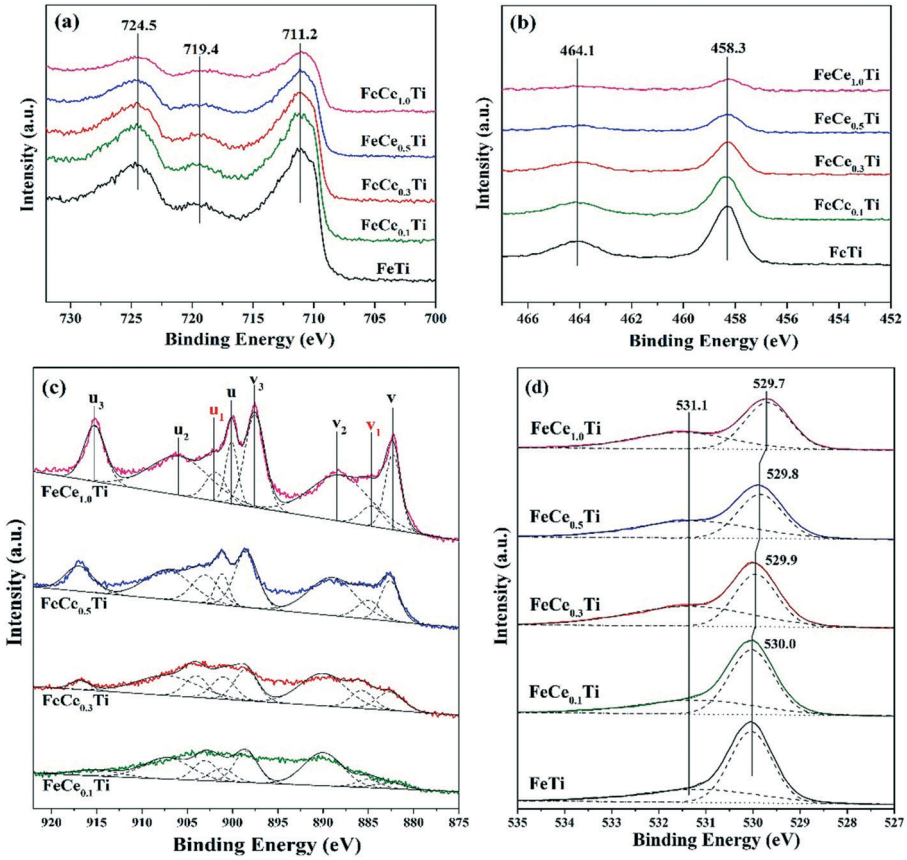

Fig. 8 XPS spectra of (a) Fe 2p, (b) Ti 2p, (c) Ce 3d, and (d) O 1s over the FeTi and $FeCe_aTi$ catalysts calcined at 500 °C.

H_2-TPR analysis. H_2-TPR experiments were conducted to investigate the reducibility of the FeTi and $FeCe_aTi$ catalysts. As shown in Fig. 9, the FeTi catalyst showed a reduction peak centered at 327 °C and a broad peak between 400 and 600 °C. The low-temperature peak was attributed to the reduction of Fe_2O_3 to Fe_3O_4, while the high-temperature one was related to further reduction of Fe_3O_4 to FeO and Fe.[3,29,61,62] Within the measured temperature range, no peak of TiO_2 was observed, indicating its poor reducibility.[10,63] Pure CeO_2 also showed weak redox ability. After Ce doping, it was noticed that the low-temperature peak shifted to higher temperature and reached the highest value for the $FeCe_{0.3}Ti$ catalyst (366 °C), and then shifted gradually toward low temperatures, indicating that $FeCe_{0.3}Ti$ exhibited the weakest reducibility. As for the standard NH_3-SCR reaction over vanadium-based catalysts, it is well accepted that the initial surface V^{5+} species are reduced to V^{4+} ones with the formation of N_2, and are then regenerated by reaction with O_2 in the gas phase to complete the catalytic cycle.[4,28] During this redox process, DFT calculations further revealed that re-oxidation of surface V^{4+} species exhibited a higher energy barrier,[64] also in agreement with the experimental results achieved by *in situ* DR-vis measurements.[5] In other words, the rate-determining step is involved in the oxidation of V^{4+} species by oxygen (V^{4+}–OH + O_2 → V^{5+}═O + H_2O), rather than the elementary steps related to the adsorption (or activation) of ammonia and the production of N_2.[5] In our case, such catalytic cycling of redox sites may also occur during the NH_3-SCR over the $FeCe_aTi$ and FeTi samples. Within the overall NH_3-SCR process, meanwhile, the regeneration of redox sites by O_2 would be the rate-determining step, the possibility of which was further confirmed by the H_2-TPR results. Specifically, the

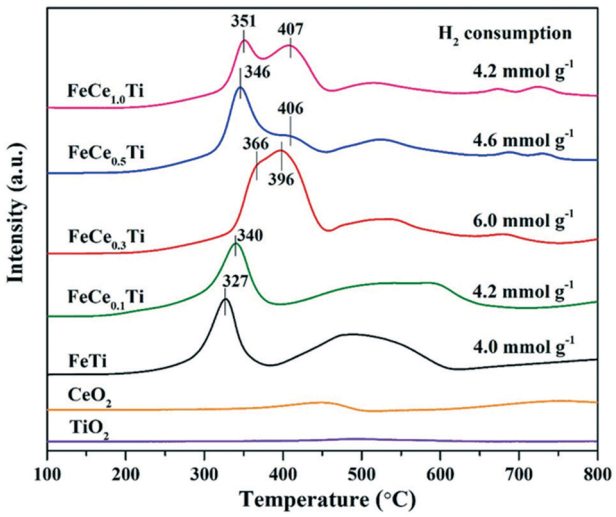

Fig. 9 H_2-TPR results of FeTi and $FeCe_aTi$ catalysts calcined at 500 °C with CeO_2 and TiO_2 as contrasts.

H_2-TPR results indicate that the $FeCe_{0.3}Ti$ catalyst exhibits a lower reducibility than FeTi, which may be a reason for its higher activation energy for NO_x reduction (Fig. 2). In addition, with an increase in the '*a*' value from 0.3 to 1.0, another peak appeared around 400 °C due to the reduction of surface oxygen related to the addition of Ce,[36] which was in accordance with the XPS and EPR results.

During the H_2-TPR process, the H_2 consumption was also calculated and is shown in Fig. 9. With increasing Ce content, the amount of H_2 consumption increased, reaching the maximum value for the $FeCe_{0.3}Ti$ catalyst, and then decreasing gradually. This trend was also in agreement with the variation in surface oxygen species ($O_\alpha/(O_\alpha + O_\beta)$) over the $FeCe_aTi$ samples listed in Table 2. Among the tested samples, it should be noted that the $FeCe_{0.3}Ti$ catalyst gave the highest number of oxygen vacancies, trapping the greatest amount of surface oxygen species. As a result, the redox sites available for NO_x reduction were richest on $FeCe_{0.3}Ti$, finally relating to the highest intrinsic activity, which was in good agreement with the kinetic study results.

The over-oxidation of NH_3 to NO is one of the main reasons for the decreased N_2 selectivity at higher temperatures. From the H_2-TPR results, it can be also speculated that the process was hindered due to the weakened redox ability of Fe^{3+} upon doping with Ce, thus achieving superior N_2 selectivity, which agrees well with the studies by Yang *et al.*[8,65] This may explain the better N_2 selectivity of $FeCe_{0.3}Ti$ compared to the other samples.

Conclusions

Compared to FeTi, the $FeCe_{0.3}Ti$ catalyst exhibited higher NO_x conversion, N_2 selectivity, and thermostability as well as higher tolerance to GHSV over the whole temperature range of NH_3-SCR measurements, despite the similar surface areas and NH_3 storage capacities of these two catalysts. With Ce doping at a proper ratio, well-dispersed Fe, Ce and Ti and rich active sites were obtained. Such changes induced by Ce introduction thus increased the amounts of active sites for NO_x adsorption and surface nitrate formation, as well as more weak-acid sites for ammonia adsorption. As a result, the L–H pathway over $FeCe_{0.3}Ti$ at low temperatures was enhanced by the introduction of Ce.

Conflicts of interest

There are no conflicts of interest to declare.

Acknowledgements

This work was financially supported by the National Key R&D Program of China (2017YFC0211105), the National Natural Science Foundation of China (21673277 and 21637005), the K. C. Wong Education Foundation, and the Strategic Priority Research Program of the Chinese Academy of Sciences (XDA23010200).

Notes and references

1 N. Apostolescu, B. Geiger, K. Hizbullah, M. T. Jan, S. Kureti, D. Reichert, F. Schott and W. Weisweiler, *Appl. Catal., B*, 2006, **62**, 104–114.
2 J. Mu, X. Li, W. Sun, S. Fan, X. Wang, L. Wang, M. Qin, G. Gan, Z. Yin and D. Zhang, *ACS Catal.*, 2018, **8**, 6760–6774.
3 D. Wang, Y. Peng, S. Xiong, B. Li, L. Gan, C. Lu, J. Chen, Y. Ma and J. Li, *Appl. Catal., B*, 2018, **221**, 556–564.
4 G. Busca, L. Lietti, G. Ramis and F. Berti, *Appl. Catal., B*, 1998, **18**, 1–36.
5 A. Marberger, D. Ferri, M. Elsener and O. Krocher, *Angew. Chem., Int. Ed.*, 2016, **55**, 11989–11994.
6 C. Li, Z. Huang, Y. Chen, X. Liu, J. Chen, W. Qu, Z. Ma and X. Tang, *ChemCatChem*, 2018, **10**, 3990–3994.
7 F. Liu, H. He and C. Zhang, *Chem. Commun.*, 2008, 2043–2045.
8 S. Yang, J. Li, C. Wang, J. Chen, L. Ma, H. Chang, L. Chen, Y. Peng and N. Yan, *Appl. Catal., B*, 2012, **117–118**, 73–80.
9 F. Liu, H. He, C. Zhang, Z. Feng, L. Zheng, Y. Xie and T. Hu, *Appl. Catal., B*, 2010, **96**, 408–420.
10 F. Liu, H. He, Y. Ding and C. Zhang, *Appl. Catal., B*, 2009, **93**, 194–204.
11 F. Liu, K. Asakura, H. He, Y. Liu, W. Shan, X. Shi and C. Zhang, *Catal. Today*, 2011, **164**, 520–527.
12 J. Liu, J. Meeprasert, S. Namuangruk, K. Zha, H. Li, L. Huang, P. Maitarad, L. Shi and D. Zhang, *J. Phys. Chem. C*, 2017, **121**, 4970–4979.
13 H. Chang, T. Zhang, H. Dang, X. Chen, Y. You, J. W. Schwank and J. Li, *Catal. Sci. Technol.*, 2018, **8**, 3313–3320.
14 F. Liu and H. He, *Catal. Today*, 2010, **153**, 70–76.
15 K. Cheng, B. Liu, W. Song, J. Liu, Y. Chen, Z. Zhao and Y. Wei, *Ind. Eng. Chem. Res.*, 2018, **57**, 7802–7810.
16 X. Gao, Y. Jiang, Y. Fu, Y. Zhong, Z. Luo and K. Cen, *Catal. Commun.*, 2010, **11**, 465–469.
17 W. Shan, F. Liu, H. He, X. Shi and C. Zhang, *Catal. Commun.*, 2011, **47**, 8046–8048.
18 W. Shan, F. Liu, H. He, X. Shi and C. Zhang, *Appl. Catal., B*, 2012, **115–116**, 100–106.
19 W. Shan, F. Liu, Y. Yu, H. He, C. Deng and X. Zi, *Catal. Commun.*, 2015, **59**, 226–228.
20 C. Tang, H. Zhang and L. Dong, *Catal. Sci. Technol.*, 2016, **6**, 1248–1264.
21 T. H. Vuong, J. Radnik, J. Rabeah, U. Bentrup, M. Schneider, H. Atia, U. Armbruster, W. Grünert and A. Brückner, *ACS Catal.*, 2017, **7**, 1693–1705.
22 R. Q. Long and R. T. Yang, *Appl. Catal., B*, 2000, **27**, 87–95.
23 S. Zhan, D. Zhu, S. Yang, M. Qiu, Y. Li, H. Yu and Z. Shen, *J. Sol-Gel Sci. Technol.*, 2014, **73**, 443–451.
24 Z. Xiong, C. Wu, Q. Hu, Y. Wang, J. Jin, C. Lu and D. Guo, *Chem. Eng. J.*, 2016, **286**, 459–466.
25 Z. Liu, Y. Liu, B. Chen, T. Zhu and L. Ma, *Catal. Sci. Technol.*, 2016, **6**, 6688–6696.
26 Y. Shu, H. Sun, X. Quan and S. Chen, *J. Phys. Chem. C*, 2012, **116**, 25319–25327.

27 Y. Shu, T. Aikebaier, X. Quan, S. Chen and H. Yu, *Appl. Catal., B*, 2014, **150-151**, 630–635.
28 J. Lai and I. E. Wachs, *ACS Catal.*, 2018, **8**, 6537–6551.
29 S. Y. Mendiola-Alvarez, A. Hernández-Ramírez, J. L. Guzmán-Mar, M. L. Maya-Treviño, A. Caballero-Quintero and L. Hinojosa-Reyes, *Catal. Today*, 2019, **328**, 91–98.
30 X. Xie, Y. Li, Z. Q. Liu, M. Haruta and W. Shen, *Nature*, 2009, **458**, 746–749.
31 Z. Ma, X. Wu, H. Härelind, D. Weng, B. Wang and Z. Si, *J. Mol. Catal. A: Chem.*, 2016, **423**, 172–180.
32 Z. Qu, L. Miao, H. Wang and Q. Fu, *Catal. Commun.*, 2015, **51**, 956–958.
33 Y. Xu, D. Zhao, X. Zhang, W. Jin, P. Kashkarov and H. Zhang, *Phys. E*, 2009, **41**, 806–811.
34 H. Wang, P. Ning, Q. Zhang, X. Liu, T. Zhang, J. Fan, J. Wang and K. Long, *Appl. Catal., A*, 2018, **561**, 158–167.
35 J. Han, J. Meeprasert, P. Maitarad, S. Nammuangruk, L. Shi and D. Zhang, *J. Phys. Chem. C*, 2016, **120**, 1523–1533.
36 Y. Cheng, J. Liu, Z. Zhao, W. Song and Y. Wei, *J. Hazard. Mater.*, 2018, **342**, 317–325.
37 P. H. C. Camargo, G. G. Nunes, G. R. Friedermann, D. J. Evans, G. J. Leigh, G. Tremiliosi-Filho, E. L. de Sá, A. J. G. Zarbin and J. s. F. Soares, *Mater. Res. Bull.*, 2003, **38**, 1915–1928.
38 R. J. G. Nuguid, D. Ferri, A. Marberger, M. Nachtegaal and O. Kröcher, *ACS Catal.*, 2019, **9**, 6814–6820.
39 Y. Inomata, S. Hata, M. Mino, E. Kiyonaga, K. Morita, K. Hikino, K. Yoshida, H. Kubota, T. Toyao, K.-i. Shimizu, M. Haruta and T. Murayama, *ACS Catal.*, 2019, **9**, 9327–9331.
40 S. Zhan, H. Zhang, Y. Zhang, Q. Shi, Y. Li and X. Li, *Appl. Catal., B*, 2017, **203**, 199–209.
41 A. Xie, Y. Tang, X. Huang, X. Jin, P. Gu, S. Luo, C. Yao and X. Li, *Chem. Eng. J.*, 2019, **370**, 897–905.
42 H. Wang, Z. Qu, S. Dong, H. Xie and C. Tang, *Environ. Sci. Technol.*, 2016, **50**, 13511–13519.
43 F. Liu, H. He, C. Zhang, W. Shan and X. Shi, *Catal. Today*, 2011, **175**, 18–25.
44 L. Chen, J. Li, M. Ge and R. Zhu, *Catal. Today*, 2010, **153**, 77–83.
45 X. Cheng, X. Zhang, D. Su, Z. Wang, J. Chang and C. Ma, *Appl. Catal., B*, 2018, **239**, 485–501.
46 L. Ren, W. Zhou, B. Sun, H. Li, P. Qiao, Y. Xu, J. Wu, K. Lin and H. Fu, *Appl. Catal., B*, 2019, **240**, 319–328.
47 Y. Yu, C. Chen, M. Ma, M. Douthwaite, C. He, J. Miao, J. Chen and C. Li, *Chem. Eng. J.*, 2019, **361**, 820–829.
48 Z. Lian, W. Shan, Y. Zhang, M. Wang and H. He, *Ind. Eng. Chem. Res.*, 2018, **57**, 12736–12741.
49 P. Wang, S. Chen, S. Gao, J. Zhang, H. Wang and Z. Wu, *Appl. Catal., B*, 2018, **231**, 299–309.
50 X. Liu, K. Zhou, L. Wang, B. Wang and Y. Li, *J. Am. Chem. Soc.*, 2009, **131**, 3140–3141.
51 M. D. Krcha, A. D. Mayernick and M. J. Janik, *J. Catal.*, 2012, **293**, 103–115.
52 L. Wei, S. Cui, H. Guo and X. Ma, *Mol. Catal.*, 2018, **445**, 102–110.
53 Y. Zhang, Z. Li, L. Zhang, L. Pan, X. Zhang, L. Wang, F. Aleem and J. Zou, *Appl. Catal., B*, 2018, **224**, 101–108.
54 H. Yu, J. Li, Y. Zhang, S. Yang, K. Han, F. Dong, T. Ma and H. Huang, *Angew. Chem., Int. Ed.*, 2019, **58**, 3880–3884.
55 T. Gu, Y. Liu, X. Weng, H. Wang and Z. Wu, *Catal. Commun.*, 2010, **12**, 310–313.
56 X. Yao, L. Chen, J. Cao, Y. Chen, M. Tian, F. Yang, J. Sun, C. Tang and L. Dong, *Chem. Eng. J.*, 2019, **369**, 46–56.
57 Q. Jin, Y. Shen, L. Ma, Y. Pan, S. Zhu, J. Zhang, W. Zhou, X. Wei and X. Li, *Catal. Today*, 2019, **327**, 279–287.
58 K. J. Lee, P. A. Kumar, M. S. Maqbool, K. N. Rao, K. H. Song and H. P. Ha, *Appl. Catal., B*, 2013, **142–143**, 705–717.
59 G. Chi, B. Shen, R. Yu, C. He and X. Zhang, *J. Hazard. Mater.*, 2017, **330**, 83–92.
60 L. J. France, Q. Yang, W. Li, Z. Chen, J. Guang, D. Guo, L. Wang and X. Li, *Appl. Catal., B*, 2017, **206**, 203–215.
61 L. Ma, J. Li, R. Ke and L. Fu, *J. Phys. Chem. C*, 2011, **115**, 7603–7612.
62 Q. Zhang, H. Wang, P. Ning, Z. Song, X. Liu and Y. Duan, *Appl. Surf. Sci.*, 2017, **419**, 733–743.
63 F. Liu and H. He, *J. Phys. Chem. C*, 2010, **114**, 16929–16936.
64 G. He, Z. Lian, Y. Yu, Y. Yang, K. Liu, X. Shi, Z. Yan, W. Shan and H. He, *Sci. Adv.*, 2018, **4**, 4637.
65 S. Yang, C. Liu, H. Chang, L. Ma, Z. Qu, N. Yan, C. Wang and J. Li, *Ind. Eng. Chem. Res.*, 2013, **52**, 5601–5610.